JOURNAL OF THERMOPHYSICS AND HEAT TRANSFER
Vol. 22, No. 2, April–June 2008

Efficient Calculation of Radiation Heat Transfer in Participating Media

P. Hassanzadeh* and G. D. Raithby†
University of Waterloo, Waterloo, Ontario N2L 3G1, Canada
and
E. H. Chui‡
National Resources Canada, Ottawa, Ontario K1A 1M1, Canada

DOI: 10.2514/1.33271

A low-cost computational solution to radiation problems can be obtained by using a simple model, such as the P_1 model, but the accuracy can be very poor. High accuracy can be obtained by solving the radiative transfer equation, but the solution cost can be exorbitant for strongly participating media. The Q_L method presented in this paper allows the radiation heat transfer to be computed from a single equation for the average intensity, like the P_1 model, but the Q_L equation contains parameters that account for a nonuniform intensity distribution. The method converges to the solution of the radiative transfer equation with grid refinement and will accommodate any scattering phase function. For a given spatial and directional discretization, and for problems involving radiation only, the accuracy of the Q_L method is shown to equal or exceed that of the finite volume method. The solution cost of the Q_L method is comparable to the finite volume method for weakly participating media, but for strongly participating media the Q_L method is much less costly. The Q_L method is designed for application in general-purpose codes in which radiation is but one of several important processes, and it is in such applications that the major benefits of the Q_L method are expected.

Nomenclature

AR	=	aspect ratio
a	=	coefficient in the algebraic equations
a_1	=	coefficient in the linear scattering phase function
B_x, B_y	=	size of the coarse-mesh block in the multigrid solver
b	=	source term in the algebraic equations
D_{ij}^l	=	defined in Eq. (23), sr
$\mathbf{e}_i$	=	unit vector in the i direction
F_i^l	=	defined in Eq. (23), sr
I	=	radiant intensity, $W/m^2 \cdot sr$
I_a	=	average intensity, $W/m^2 \cdot sr$
I_b	=	blackbody intensity, $W/m^2 \cdot sr$
$\mathbf{I}_s$	=	scattering integral, W/m^2
$\mathbf{I}_t$	=	transport integral, W/m^3
I_P^l	=	intensity at node P within ω^l, $W/m^2 \cdot sr$
K	=	absorption coefficient, m^{-1}
L	=	total number of discrete solid angles
L_x, L_y	=	dimensions of a rectangular enclosure, m
N_x, N_y	=	number of control volumes in the x and y directions
N_θ, N_ϕ	=	number of discrete solid angles in the θ and ϕ directions
N_i^l	=	defined in Eq. (29), sr
$\mathbf{n}$	=	unit surface normal, out of medium
q	=	net surface heat flux, W/m^2
$\mathbf{q}$	=	radiant heat flux vector [Eq. (9)], W/m^2
q_R	=	incident radiant heat flux onto a surface, W/m^2
R	=	residual in each cycle [Eqs. (31) and (34)]
Rng	=	range of intensity in the domain
r	=	residual in each multigrid iteration [Eq. (32)]
$\mathbf{r}$	=	spatial position vector, m
S	=	surface area, m^2
S_i	=	defined in Eq. (25), sr
s	=	distance along a beam in the $\mathbf{s}$ direction, m
$\mathbf{s}$	=	unit vector in the direction of intensity
s_i	=	component of $\mathbf{s}$ in direction $\mathbf{e}_i$
$\mathbf{s}^l$	=	unit direction vector in the center of discrete solid angle ω^l
T	=	temperature, K
T_G	=	temperature of the medium, K
T_h, T_c	=	temperature of the hot and cold walls, K
T_{ij}	=	defined in Eq. (25), sr
$T_{\max}$, $T_{\min}$	=	maximum and minimum wall temperatures, K
V	=	volume, m^3
x, y, z	=	Cartesian coordinates, m
x_i	=	distance in the $\mathbf{e}_i$ direction, m
α^l	=	phase weight [Eq. (20)]
Δ	=	width of the interior control volumes in a uniform grid, m
ϵ	=	emissivity
θ	=	polar angle measured from the z axis, rad
κ	=	extinction coefficient ($K + \sigma^s$), m^{-1}
κ^*	=	optical thickness (κL_y)
ρ	=	reflectivity
σ	=	Stefan–Boltzmann constant ($=5.729 \times 10^{-8}$ $W/m^2 \cdot K^4$)
σ^s	=	scattering coefficient, m^{-1}
$\Phi(\mathbf{s}', \mathbf{s})$	=	phase function for scattering from $\mathbf{s}'$ to $\mathbf{s}$
$\bar{\Phi}^{l'l}$	=	defined in Eq. (5), sr
ϕ	=	azimuthal angle in the x–y plane measured from the x axis, rad
Ψ	=	scattering angle between incident ($\mathbf{s}'$) and scattered ($\mathbf{s}$) directions, rad

Paper 2008-4244 to be presented at the 40th AIAA Thermophysics Conference, Seattle, Washington, 23–26 June 2008; received 5 July 2007; revision received 10 December 2007; accepted for publication 18 January 2008.

*Graduate Research Assistant, Department of Mechanical and Mechatronics Engineering. Student Member AIAA.
†Distinguished Professor Emeritus, Department of Mechanical and Mechatronics Engineering; graith@mecheng1.uwaterloo.ca (Corresponding Author).
‡Senior Research Scientist, CANMET Energy Technology Centre.

Ω	=	scattering albedo (σ^s/κ)
ω	=	solid angle, sr
ω^+	=	range of solid angles pointing from wall to medium, sr
ω^-	=	range of solid angles pointing from medium to wall, sr

Subscripts

B	=	at the bottom wall
i	=	in the $\mathbf{e}_i$ direction
ip	=	at the integration point
j	=	in the $\mathbf{e}_j$ direction
nb	=	associated with neighbors of node P
P	=	at node P
s	=	surface
T	=	at the top wall
x	=	in the x direction
y	=	in the y direction

Superscripts

l	=	associated with discrete solid angle ω^l
o	=	residual in the first iteration or cycle
$*$	=	dimensionless

I. Introduction

GENERAL purpose computational fluid dynamics (CFD) codes are now widely used to solve complex problems that often involve fluid flow, combustion, particle generation and motion, and heat transfer by conduction/convection and by radiation. The conservation of radiant energy is expressed by the radiative transfer equation (RTE) with intensity as the dependent variable. Intensity is, in general, a 6-dimensional variable (it depends on wavelength, three spatial locations, and two directions). When particles in the medium are the main contributors to radiation, and for most surfaces, the dependence on wavelength can be reasonably ignored so the radiation can be approximated as gray, thereby reducing the dimensionality to 5. Viskanta and Mengüç [1] and Modest [2] give a clear introduction to the main solution methods.

To obtain the solution of the RTE in CFD codes, the discrete ordinates method (DOM) [3–6] and the finite volume method (FVM) [7–10] are natural choices because they can use the same spatial mesh as for velocity, pressure, temperature, and other variables. But even if the gray approximation is made, the solution using these methods can present a formidable computational challenge. If, for example, 48 directions are required to approximate the actual directional distribution of intensity, then 48 equations must be formed and solved for each node. If these equations are weakly coupled, the computer resources required may be reasonable. But the 48 equations may be strongly coupled through scattering, wall reflection, and interaction with the internal energy equation for temperature. In the conventional solution procedure, referred to here as *explicit update*, the intensity equation in each direction is solved in isolation, using the best available intensities in the other directions. When the interdirectional coupling is strong, this procedure converges so slowly that resources on even the largest computer can be quickly saturated [1,7].

Because of this barrier, research has been directed at accelerating the solution for the directional intensities. Fiveland and Jessee [11] reviewed the methods developed in the neutron transport literature and established that, of these, the mesh rebalance method was superior when applied to the DOM for thermal radiation. They then showed that the method sometimes failed entirely for fine meshes and for a range of optical thicknesses. A modified method called coarse-mesh rebalance performed well for their simple test problems, but can also become unstable [12]. Chui and Raithby [13] developed a similar acceleration method for the FVM, and explained why divergence occurs [14], but did not provide a generally applicable recipe.

In another approach, Mathur and Murthy [15,16] obtained impressive reductions in solution times for problems with strong directional coupling by implementing the coupled ordinates method (COMET). They applied a multigrid solver where, at each mesh level, directional intensities and temperature corrections at each node were solved together by the inversion of a local matrix. To optimize this point inversion for the interior nodes, they included the average intensity in the solution which resulted in a matrix that is easily upper triangularized. Their inversion is not applicable to complex scattering phase functions and to nodes adjacent to the boundary. Drawbacks of the method, when applied in a multiprocess CFD calculation, include complexity, and the inability to handle general scattering phase functions. Also to include the effect of radiation on every time step, all directional intensities must be updated; even with the improved solution method, this is expensive.

The present paper introduces the Q_L method that is intended for use in multiprocess CFD codes. This method forms a single equation for the average intensity I_a, which contains L parameters (called the phase weights) that account for different intensities in L directions. The phase weights are obtained by solving for the directional intensities I^l, $l = 1, 2, \ldots, L$, using the FVM, but in a way that uses the I_a solution of the Q_L equations to avoid the slow convergence associated with the interdirectional coupling of intensities. When solving for radiation alone, uncoupled from other processes, and when there is strong coupling among the directional intensities, this approach proves to be much less costly than the application of the FVM alone. This paper applies the Q_L method to several problems involving radiation only.

Although it is not demonstrated in this paper, it is reasonable to expect that the greatest benefits will accrue when the Q_L method is employed in a general-purpose code applied to multiprocess problems. The reasons are given in the Discussion section.

The FVM is first briefly reviewed and the Q_L method is derived in detail and applied to several radiation problems. The cost and accuracy of the Q_L method are then compared to the FVM with explicit updates for several problems.

II. Theory

A. Radiative Transfer Equation

For gray radiation, the radiative heat transfer at location $\mathbf{r}$ in a solid angle $d\omega$ which lies in the direction of the unit vector $\mathbf{s} = s_i\mathbf{e}_i$ is described by the RTE [2]:

$$\frac{dI(\mathbf{r},\mathbf{s})}{ds} = -(K+\sigma^s)I(\mathbf{r},\mathbf{s}) + KI_b(\mathbf{r}) + \frac{\sigma^s}{4\pi}\int_{4\pi} I(\mathbf{r},\mathbf{s}')\Phi(\mathbf{s}',\mathbf{s})\,d\omega' \tag{1}$$

where K is the absorption coefficient, σ^s the scattering coefficient, I_b the blackbody intensity, and $\Phi(\mathbf{s}',\mathbf{s})$ the scattering phase function. The last term is called the in-scattering term. Radiation is coupled with the internal energy equation through the absorption term $-KI(\mathbf{r},\mathbf{s})$ and emission term $KI_b(\mathbf{r})$. If there is no convective and conductive heat transfer, the medium will adjust its temperature to make the total absorbed and emitted energy balance, so that

$$-K\int_{4\pi} I\,d\omega + K\int_{4\pi} I_b\,d\omega = 0$$

or

$$I_b = \left(\frac{1}{4\pi}\int_{4\pi} I\,d\omega \equiv I_a\right) \tag{2}$$

where I_a is the average intensity.

B. Finite Volume Method

FVM Equations: The FVM is briefly reviewed because it is used in the Q_L method (to provide phase weights), and because the cost and accuracy of the Q_L and FVM are compared in the Results section. The method has been discussed at length in the literature [2,7,9].

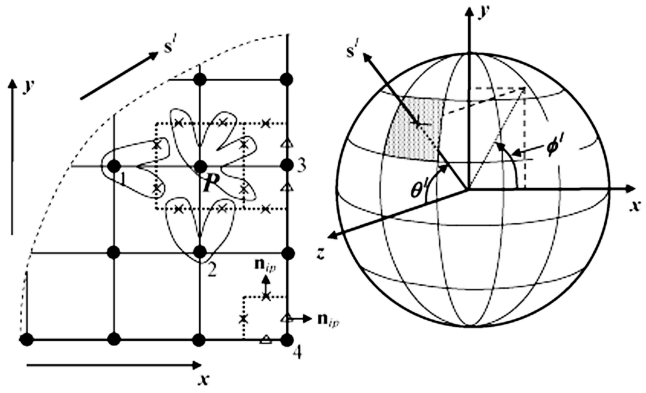

a) b)

Fig. 1 a) Spatial control volumes surrounding nodes on a 2-D Cartesian mesh, and b) solid angles for directional discretization.

The application of any finite volume scheme can begin by integrating the differential conservation equation over a discrete range of its independent variables. For radiation, the intensity depends on spatial location and on direction, so that the generalized *volume* consists of a spatial volume V_P surrounding node P, and a discrete solid angle ω^l with unit vector $\mathbf{s}^l$ through its center.

A simple example is shown in Fig. 1. The spatial volumes surrounding an interior node P, a boundary node "3," and a corner node "4" are denoted by dotted lines. Figure 1b shows direction subdivided into L solid angles ω^l, $l = 1, 2, \ldots, L$. Solid angle ω^l spans a polar angle of $\Delta\theta^l = \pi/N_\theta$ and an azimuthal angle $\Delta\phi^l = 2\pi/N_\phi$, where N_θ and N_ϕ are the number of solid angles in the θ and ϕ directions, respectively.

Integrating Eq. (1) over a volume V_P with surface area S_P associated with any node P, and over the solid angle ω^l, results in the integral conservation equation [7]:

$$\int_{S_P} \mathbf{q}^l \cdot \mathbf{n}\, \mathrm{d}S = \int_{V_P}\int_{\omega^l} (-(K+\sigma^s) I(\mathbf{r},\mathbf{s}) + K I_b(\mathbf{r}))\, \mathrm{d}\omega\, \mathrm{d}V + \int_{V_P}\int_{\omega^l} \left(\frac{\sigma^s}{4\pi} \int_{4\pi} I(\mathbf{r},\mathbf{s}')\Phi(\mathbf{s}',\mathbf{s})\, \mathrm{d}\omega' \right) \mathrm{d}\omega\, \mathrm{d}V \tag{3}$$

where

$$\mathbf{q}^l = \int_{\omega^l} I(\mathbf{r},\mathbf{s})\mathbf{s}\, \mathrm{d}\omega$$

is the *radiant heat flux vector* for radiation within the solid angle ω^l.

The right-hand side, RHS, of Eq. (3) is approximated by treating I, I_b, K, and σ^s as constant over V_P and ω^l, which results in

$$\mathrm{RHS} \approx \left[-\left(K_P + \sigma_P^s\right) I_P^l + K_P I_{b,P} + \frac{\sigma_P^s}{4\pi} \sum_{l'} I_P^{l'} \bar{\Phi}^{l'l} \right] V_P \omega^l \tag{4}$$

where [17]

$$\bar{\Phi}^{l'l} = \frac{\int_{\omega^l}\int_{\omega^{l'}} \Phi(\mathbf{s}',\mathbf{s})\, \mathrm{d}\omega'\, \mathrm{d}\omega}{\omega^l} \tag{5}$$

is obtained by analytical or precise numerical integration for any phase function.

To evaluate the left-hand side, LHS, of Eq. (3)

$$\mathrm{LHS} = \sum_{\mathrm{ip}} \int_{S_{\mathrm{ip}}} \mathbf{q}^l \cdot \mathbf{n}\, \mathrm{d}S \approx \sum_{\mathrm{ip}} \mathbf{q}_{\mathrm{ip}}^l \cdot \mathbf{n}_{\mathrm{ip}} S_{\mathrm{ip}} \approx \sum_{\mathrm{ip}} I_{\mathrm{ip}}^l \mathbf{N}^l \cdot \mathbf{n}_{\mathrm{ip}} S_{\mathrm{ip}} \tag{6}$$

where

$$\mathbf{N}^l = \int_{\omega^l} \mathbf{s}\, \mathrm{d}\omega$$

is obtained by analytical integration and stored, S_{ip} is the surface area of the panel containing integration point "ip," and I_{ip}^l and $\mathbf{n}_{\mathrm{ip}}$ are the intensity and unit outward surface normal at "ip." The integration points are denoted in Fig. 1a by $\times$ for interior panels and by $\triangle$ for boundary panels.

To provide equations for the nodal intensities, each I_{ip}^l must be expressed in terms of the nodal values of I^l. There is a large body of literature that explores many alternatives [6,18,19]. Schemes that are second order accurate $[\mathcal{O}(\Delta^2)]$ are desirable, but are either more expensive than $\mathcal{O}(\Delta)$ schemes to solve or may produce numerical dispersion (over- and undershoots) in the intensity distribution. The main focus of this paper is the cost of predicting radiation heat transfer by the Q_L method. To compare the Q_L method with the least expensive and most easily replicated FVM, the first-order upstream difference scheme (UDS) [9,18] (also called the step scheme) is used. For the $\mathbf{s}^l$ direction shown in Fig. 1a, I_{ip}^l for the four "downstream" integration points are approximated by I_P^l, as denoted by the envelope enclosing these points and node P. I_{ip}^l at "upstream" integration points, at which $\mathbf{s}^l \cdot \mathbf{n}_{\mathrm{ip}} < 0$, are approximated by I^l at upstream nodes (I_1^l and I_2^l), as shown. Substituting these approximations into Eq. (6), and then substituting the LHS and RHS approximations into Eq. (3) gives an algebraic equation for each interior node and for each solid angle of the form

$$a_P^l I_P^l + \sum_{\mathrm{nb}} a_{\mathrm{nb}}^l I_{\mathrm{nb}}^l = b_P^l \tag{7}$$

The control volumes for boundary nodes, like nodes 3 and 4 in Fig. 1a, have some interior surface panels, and some boundary surface panels. The closure relations are the same for the interior integration points, and for the boundary integration points where $\mathbf{s}^l \cdot \mathbf{n}_{\mathrm{ip}} > 0$ (the upstream node is the control volume node in this case). For $\mathbf{s}^l \cdot \mathbf{n}_{\mathrm{ip}} < 0$, the intensity I_{ip}^l that enters the domain is the sum of the surface-emitted radiation and the radiation reflected within ω^l. When all terms are assembled, the intensities at the boundary nodes are again given by Eq. (7).

C. Q_L Method

The Q_L method (the Q_L method was originally proposed in notes of the second author dated June 1996) [20] begins by integrating the RTE over a volume V_P and over all directions, giving rise to the radiation energy equation

$$\int_{S_P} \mathbf{q}(\mathbf{r}) \cdot \mathbf{n}\, \mathrm{d}S = 4\pi \left[\int_{V_P} K I_b\, \mathrm{d}V - \int_{V_P} K I_a\, \mathrm{d}V \right] \tag{8}$$

where the Gauss divergence theorem has been used on the left side and the scattering terms have exactly canceled (because scattering only redistributes radiation, it is not a source or sink of radiant energy). The average intensity is

$$I_a = \frac{1}{4\pi} \int_{4\pi} I\, \mathrm{d}\omega$$

and $\mathbf{q}(\mathbf{r})$ is the radiant heat flux vector defined as

$$\mathbf{q}(\mathbf{r}) = \int_{4\pi} I(\mathbf{r},\mathbf{s})\mathbf{s}\, \mathrm{d}\omega \tag{9}$$

The finite volume approximation of Eq. (8) is

$$\sum_{\mathrm{ip}} \mathbf{q}_{\mathrm{ip}} \cdot \mathbf{n}_{\mathrm{ip}} S_{\mathrm{ip}} = 4\pi K_P [I_{b,P} - I_{a,P}] V_P \tag{10}$$

The value of $I_{b,P} = \sigma T_P^4/\pi$ is, in general, provided by the internal energy equation, but for radiative equilibrium the right side of Eq. (10) vanishes because $I_b = I_a$, as already discussed. If Eq. (10) is to be useful, $\mathbf{q}_{\mathrm{ip}}$ must be expressed in terms of the nodal values of I_a. The procedure used to obtain this relation is the key feature of the Q_L method.

Equation for $\mathbf{q}(\mathbf{r})$: To obtain the required equation for $\mathbf{q}(\mathbf{r})$, a relation for $I(\mathbf{r},\mathbf{s})$ is required in Eq. (9). This is obtained by rearranging the RTE, Eq. (1), as follows:

$$I(\mathbf{r},\mathbf{s}) = \frac{-1}{\kappa}\frac{\mathrm{d}I}{\mathrm{d}s} + (1-\Omega)I_b(\mathbf{r}) + \Omega\left\{\frac{1}{4\pi}\int_{4\pi} I(\mathbf{r},\mathbf{s}')\Phi(\mathbf{s}',\mathbf{s})\,\mathrm{d}\omega'\right\} \tag{11}$$

where $\kappa = K + \sigma^s$ is the extinction coefficient and $\Omega = \sigma^s/\kappa$ is the scattering albedo. This equation becomes inappropriate in the $\kappa \to 0$ limit because each term on the right side of Eq. (11) becomes indeterminate. This issue will be addressed in the Results section.

Substituting Eq. (11) for $I(\mathbf{r},\mathbf{s})$ into Eq. (9) results in

$$\mathbf{q}\,(\mathbf{r}) = -\frac{1}{\kappa}\mathbf{I}_t + \Omega\mathbf{I}_s \tag{12}$$

where $\mathbf{I}_t$, the *transport integral*, and $\mathbf{I}_s$, the *scattering integral*, are given by

$$\mathbf{I}_t = \left\{\int_{4\pi}\frac{\partial I}{\partial x_j}s_j s_i\,\mathrm{d}\omega\right\}\mathbf{e}_i \tag{13}$$

$$\mathbf{I}_s = \left\{\int_{4\pi}\left[\frac{1}{4\pi}\int_{4\pi} I(\mathbf{r},\mathbf{s}')\Phi(\mathbf{s}',\mathbf{s})\,\mathrm{d}\omega'\right]s_i\,\mathrm{d}\omega\right\}\mathbf{e}_i \tag{14}$$

$\mathbf{e}_i$ is the unit Cartesian basis vector in the x_i direction, and a repeated index implies summation. The $s_i s_j$ product has the property that

$$\begin{aligned}\int_{4\pi} s_i s_j\,\mathrm{d}\omega &= \frac{4\pi}{3} \quad \text{for } i=j\\ &= 0 \quad \text{for } i\neq j\end{aligned} \tag{15}$$

Before giving general approximations for $\mathbf{I}_t$ and $\mathbf{I}_s$, some interesting special cases are examined.

Isotropic Intensity: If, for the purpose of evaluating the transport integral $\mathbf{I}_t$, intensity is taken as isotropic [Note that this is different than using an isotropic intensity in Eq. (9), where $\mathbf{q}(\mathbf{r}) = 0$ results.], $I(\mathbf{r},\mathbf{s}) \approx I_a(\mathbf{r})$, Eq. (13) gives

$$\mathbf{I}_t = \left\{\int_{4\pi}\frac{\partial I}{\partial x_j}s_j s_i\,\mathrm{d}\omega\right\}\mathbf{e}_i \approx \frac{\partial I_a}{\partial x_j}\left\{\int_{4\pi} s_j s_i\,\mathrm{d}\omega\right\}\mathbf{e}_i = \frac{4\pi}{3}\nabla I_a \tag{16}$$

where $\nabla(\,) = [\partial(\,)/\partial x_i]\mathbf{e}_i$ is the gradient operator. For $I \approx I_a$ *or* for isotropic scattering $[\Phi(\mathbf{s}',\mathbf{s}) = 1]$, Eq. (14) gives $\mathbf{I}_s = 0$. Equation (12) for $\mathbf{q}$ reduces to

$$\mathbf{q} = -\frac{4\pi}{3\kappa}\nabla I_a \tag{17}$$

This is the P_1 approximation usually obtained from the leading terms of a spherical harmonics expansion [2].

Linear Anisotropic Scattering: For $\Phi(\mathbf{s}',\mathbf{s}) = 1 + a_1(\mathbf{s}'\cdot\mathbf{s})$, the uniform part of $\Phi(\mathbf{s}',\mathbf{s})$ does not contribute to the scattering integral. The resulting exact equation for $\mathbf{I}_s$ is

$$\begin{aligned}\mathbf{I}_s &= \frac{a_1}{4\pi}\int_{4\pi}\left\{\int_{4\pi} I(\mathbf{r},\mathbf{s}')\mathbf{s}\cdot\mathbf{s}'\,\mathrm{d}\omega'\right\}\mathbf{s}\,\mathrm{d}\omega\\ &= \frac{a_1}{4\pi}\left\{\int_{4\pi} I(\mathbf{r},\mathbf{s}')\left[\int_{4\pi} s_i s_j\,\mathrm{d}\omega\right]s'_j\,\mathrm{d}\omega'\right\}\mathbf{e}_i = \frac{a_1}{3}\mathbf{q}(\mathbf{r})\end{aligned} \tag{18}$$

Substituting this into Eq. (12), for any intensity distribution

$$\mathbf{q}\,(\mathbf{r}) = \frac{-1}{\kappa(1-a_1\Omega/3)}\mathbf{I}_t \tag{19}$$

For approximately isotropic intensity, inserting Eq. (16) into Eq. (19) gives the approximation

$$\mathbf{q}\,(\mathbf{r}) = \frac{-4\pi}{3\kappa(1-a_1\Omega/3)}\nabla I_a$$

used in the P_1 model.

General Approximation for $\mathbf{q}(\mathbf{r})$: Eqs. (13) and (14) for $\mathbf{I}_t$ and $\mathbf{I}_s$ can be approximated in terms of I_a and the phase weight α^l defined as

$$\alpha^l = I^l/I_a \tag{20}$$

If it is assumed that the phase weights are known, applying $I^l = \alpha^l I_a$ in Eqs. (13) and (14) gives

$$\begin{aligned}\mathbf{I}_t &= \left\{\int_{4\pi}\frac{\partial I}{\partial x_j}s_j s_i\,\mathrm{d}\omega\right\}\mathbf{e}_i = \frac{\partial}{\partial x_j}\left\{\int_{4\pi} I s_i s_j\,\mathrm{d}\omega\right\}\mathbf{e}_i\\ &\approx \frac{\partial}{\partial x_j}\left\{I_a\sum_{l=1}^{L}\alpha^l\left[\int_{\omega^l} s_i s_j\,\mathrm{d}\omega\right]\right\}\mathbf{e}_i = \frac{\partial}{\partial x_j}\left\{I_a\sum_{l=1}^{L}\alpha^l D_{ij}^l\right\}\mathbf{e}_i\end{aligned} \tag{21}$$

$$\begin{aligned}\mathbf{I}_s &= \int_{4\pi}\left\{\frac{1}{4\pi}\int_{4\pi} I(\mathbf{r},\mathbf{s}')\Phi(\mathbf{s}',\mathbf{s})\,\mathrm{d}\omega'\right\}\mathbf{s}\,\mathrm{d}\omega\\ &\approx I_a(\mathbf{r})\sum_{l'=1}^{L}\alpha^{l'}\left[\int_{\omega^{l'}}\left\{\frac{1}{4\pi}\int_{4\pi}\Phi(\mathbf{s}',\mathbf{s})s_i\,\mathrm{d}\omega\right\}\mathrm{d}\omega'\right]\mathbf{e}_i\\ &= I_a(\mathbf{r})\sum_{l'=1}^{L}\alpha^{l'}F_i^{l'}\mathbf{e}_i = I_a(\mathbf{r})\sum_{l=1}^{L}\alpha^l F_i^l\mathbf{e}_i\end{aligned} \tag{22}$$

where

$$D_{ij}^l = \int_{\omega^l} s_i s_j\,\mathrm{d}\omega \quad \text{and} \quad F_i^l = \int_{\omega^l}\left\{\frac{1}{4\pi}\int_{4\pi}\Phi(\mathbf{s}',\mathbf{s})s'_i\,\mathrm{d}\omega'\right\}\mathrm{d}\omega \tag{23}$$

are independent of the spatial location and are calculated analytically or by precise numerical integration and stored. The heat flux vector at $\mathbf{r}$ is therefore obtained by substituting Eqs. (21) and (22) into Eq. (12) to obtain the following equation for the radiant heat flux vector:

$$\mathbf{q} = \left[-\frac{1}{\kappa}\frac{\partial}{\partial x_j}\left(I_a\sum_{l=1}^{L}\alpha^l D_{ij}^l\right) + \Omega\left(I_a\sum_{l=1}^{L}\alpha^l F_i^l\right)\right]\mathbf{e}_i \tag{24}$$

Defining

$$T_{ij} = \sum_{l=1}^{L}\alpha^l D_{ij}^l \quad \text{and} \quad S_i = \sum_{l=1}^{L}\alpha^l F_i^l \tag{25}$$

the value of $\mathbf{q}_{\mathrm{ip}}$ at each integration point required in Eq. (10) is given by

$$\mathbf{q}_{\mathrm{ip}} = \left\{-\frac{1}{\kappa_{\mathrm{ip}}}\left(\frac{\partial}{\partial x_j}(T_{ij}I_a)\right)_{\mathrm{ip}} + \Omega_{\mathrm{ip}}(S_i I_a)_{\mathrm{ip}}\right\}\mathbf{e}_i \tag{26}$$

At each integration point, the values of κ_{ip} and Ω_{ip} are obtained from nodal values by linear interpolation within the element, and equations that relate $[(\partial/\partial x_j)(T_{ij}I_a)]_{\mathrm{ip}}$ and $(S_i I_a)_{\mathrm{ip}}$ to nodal values of I_a are obtained using bilinear shape functions [20,21].

For integration points that lie on the boundary of a gray-diffuse surface

$$\begin{aligned}\mathbf{q}_{\mathrm{ip}}\cdot\mathbf{n}_{\mathrm{ip}} &= \int_{\omega^-} I_{\mathrm{ip}}\mathbf{s}\cdot\mathbf{n}_{\mathrm{ip}}\,\mathrm{d}\omega - \rho_s\int_{\omega^-} I_{\mathrm{ip}}\mathbf{s}\cdot\mathbf{n}_{\mathrm{ip}}\,\mathrm{d}\omega\\ &\quad + \epsilon_s\frac{\sigma T_s^4}{\pi}\int_{\omega^+}\mathbf{s}\cdot\mathbf{n}_{\mathrm{ip}}\,\mathrm{d}\omega = \epsilon_s\int_{\omega^-} I_{\mathrm{ip}}\mathbf{s}\cdot\mathbf{n}_{\mathrm{ip}}\,\mathrm{d}\omega - \epsilon_s\sigma T_s^4\end{aligned} \tag{27}$$

where ω^+ is the range of solid angles carrying radiation into the medium from the surface, and ω^- is the range carrying radiation out of the medium toward the surface. ρ_s is the surface reflectivity, $\rho_s = 1 - \epsilon_s$, and

$$\int_{\omega^+=2\pi} \mathbf{s}\cdot\mathbf{n}_{\text{ip}}\,\mathrm{d}\omega = -\pi$$

In the discrete form, I_{ip} in Eq. (27) is approximated by $I_P^l = \alpha_P^l I_{a,P}$ which yields the boundary integration-point heat flux

$$\mathbf{q}_{\text{ip}}\cdot\mathbf{n}_{\text{ip}} = q_{\text{ip}} \approx \epsilon_s I_{a,P} \sum_{\mathbf{N}^l\cdot\mathbf{n}_{\text{ip}}>0} \alpha_P^l N_i^l \mathbf{e}_i\cdot\mathbf{n}_{\text{ip}} - \epsilon_s\sigma T_s^4 \tag{28}$$

where

$$N_i^l = \int_{\omega^l} s_i\,\mathrm{d}\omega \tag{29}$$

Substituting Eq. (26) for interior integration points and Eq. (28) for boundary integration points into Eq. (10) results in an algebraic equation for I_a of the form

$$a_P I_{a,P} + \sum_{\text{nb}} a_{\text{nb}} I_{a,\text{nb}} = b_P \tag{30}$$

where the coefficients and the source term depend on α^l. In general, the α^l distribution is not known and must be provided by one of the methods which solve the RTE to find the directional intensities. As already mentioned, in this paper the FVM with UDS has been adopted to obtain the directional intensity distribution.

D. Solution Procedure

Results from the FVM (with UDS and explicit update) and the Q_L method are presented in the next section for several benchmark problems in which radiation is solved in isolation by assuming a known temperature field or invoking the radiative equilibrium approximation [Eq. (2)]. Details relating to the solution method for this special case are now presented.

FVM Solution with Explicit Update: The FVM is implemented by solving Eq. (7) for each directional I^l, holding intensities in other directions at their most recently calculated values. The average intensity,

$$I_a = \sum_L I^l\omega^l/4\pi$$

is then calculated and the RHS in Eq. (4) is updated. This process is repeated until convergence is achieved. One update of all I_P^l and I_a is defined as one FVM cycle.

Convergence is judged by calculating the residual R as the maximum of the scaled residual of Eq. (7) calculated over all nodes P and directions l:

$$R = \max\left\{\frac{|a_P^l I_P^l + \sum_{\text{nb}} a_{\text{nb}}^l I_{\text{nb}}^l - b_P^l|}{a_P^l \times \text{Rng}}\right\} \tag{31}$$

R is calculated after the coefficients have been updated, but before the new intensities based on these coefficients have been calculated. Rng is the range of intensity in the domain where $\sigma(T_{\max}^4 - T_{\min}^4)/\pi$ is used here ($T_{\max}$ and $T_{\min}$ are the maximum and minimum wall temperatures). On the first cycle all values of I_P^l are initialized to 10^{-5} W/m$^2\cdot$sr and the residual R is stored as R^o. The cycles are repeated until the convergence criterion $R/R^o \le 10^{-5}$ is reached.

Q_L *Solution*: One Q_L cycle (for radiation-only problems) consists of one solution of the I_a equations [Eq. (30)], and one solution of the FVM equations for I^l [Eq. (7)]. Equation (30) for I_a is solved using the additive correction multigrid (ACM) solver of Hutchinson and Raithby [22] using a V-cycle [23] with one Gauss–Seidel smoothing for each restriction and prolongation. The control volumes for each coarse grid are formed by agglomerating $B_x \times B_y$ control volumes of the finer mesh, where B_x and B_y are usually 2 or 3. Coarsening is continued until no further agglomeration is possible. Iteration of the I_a equations is terminated when $r/r^o \le 10^{-5}$, where

$$r = \max\left\{\frac{|a_P I_{a,P} + \sum_{\text{nb}} a_{\text{nb}} I_{a,\text{nb}} - b_P|}{a_P \times \text{Rng}}\right\} \tag{32}$$

is calculated at the end of each iteration (when the V-cycle is done) and r^o is r on the first iteration. Rng is calculated in the same way as before.

To obtain α^l, the average intensities from the solution to the I_a equations are now used, instead of

$$I_a = \sum_L I^l\omega^l/4\pi$$

in the FVM equations: the wall reflection and the in-scattering term [the third term in Eq. (4)] are updated using the new values of I_a and the previous-cycle values of α^l. In the case of radiative equilibrium, the second term in Eq. (4) is also updated from $I_b = I_a$. This eliminates the interdirectional coupling of the I^l equations, allowing the FVM equation for each I^l to be formed and solved in a single sweep of the mesh. This is important because the slow convergence of the FVM for strong interdirectional coupling is avoided. When the new directional intensities are obtained, the α^l distribution is updated:

$$\alpha_P^l = \frac{I_P^l}{\frac{1}{4\pi}\sum_L I_P^l\omega^l} \tag{33}$$

Therefore, for radiative equilibrium, the solution procedure is as follows:

1) D_{ij}^l, F_i^l, and N_i^l ($i, j = 1, 2, 3$) are calculated from Eqs. (23) and (29) and stored.

2) $\alpha^l = 1$ and $I_a = 10^{-5}$ W/m^2 sr are used as initial guess. Then T_{ij} and S_i are calculated from Eq. (25) and the coefficients and the source term in Eq. (30) are obtained.

3) Equation (30) is solved for new values of I_a by the ACM to achieve $r/r^o \le 10^{-5}$.

4) Knowing the new I_a and old α^l distributions, the I_b and in-scattering terms in Eq. (4) and wall reflection are updated.

5) Equation (7) is solved for I^l by sweeping the grid once for each direction l . The α^l distribution is then updated by Eq. (33).

6) T_{ij} and S_i are updated from Eq. (25) and the coefficients and the source term in Eq. (30) are calculated.

7) Steps 3 to 6 (Q_L cycle) are repeated until a preset convergence criterion is satisfied.

The convergence criterion for the Q_L cycle is $R/R^o \le 10^{-5}$ where R, calculated in step 7, is defined as the maximum scaled residual of Eq. (30) over all nodes:

$$R = \max\left\{\frac{|a_P I_{a,P} + \sum_{\text{nb}} a_{\text{nb}} I_{a,\text{nb}} - b_P|}{a_P \times \text{Rng}}\right\} \tag{34}$$

and R^o is R on the first cycle.

As an alternative to Eq. (31) for the FVM and Eq. (34) for the Q_L method, convergence could require that the maximum relative change in average intensity between cycles be less than 10^{-5} (i.e., $\max[|I_{a,P}^{\text{new}} - I_{a,P}^{\text{old}}|/I_{a,P}^{\text{old}}] < 10^{-5}$) Using this criterion, the number of cycles to achieve convergence was very similar to using Eqs. (31) and (34).

III. Results

The Q_L method has been applied to several 1-D and 2-D benchmark problems and its accuracy, convergence rate, and solution cost are compared to the FVM applied using UDS and explicit update. Also its accuracy is compared with the accuracy of the P_1 model. The geometry of the solved test cases is a two-dimensional $L_x \times L_y$ rectangular enclosure with isothermal diffuse-gray walls where the wall temperature and emissivity are constant and known. The enclosed gray medium has known and uniform K,

σ^s, and $\Phi(\mathbf{s}', \mathbf{s})$, and has temperature T_G that is either known or determined by the radiation field (i.e., radiative equilibrium). The origin of the coordinate system is located at the left-bottom corner of the enclosure and aspect ratio is defined as $AR = L_y/L_x$. A vertex-centered finite volume Cartesian grid with $N_x \times N_y$ control volumes is applied to discretize the equations.

The FVM and Q_L results must approach the exact solution of the RTE as the spatial and angular meshes are refined. For large multiprocess problems, it is not always practical to refine the mesh to obtain grid independence. The *accuracy* of the FVM and the Q_L method are therefore reported for fairly coarse meshes for each problem. To properly understand the *solution cost*, fairly fine grids are required because a very coarse grid can sometimes lead to an anomalous fast convergence. Note that in the context of this paper, cost means the solution time in serial computation.

To report the results, several dimensionless parameters have been defined and used for all problems:

1) Nondimensional distance: $x^* = x/L_x$ and $y^* = y/L_y$.

2) Optical thickness: $\kappa^* = \kappa L_y$.

3) Nondimensional heat flux at the bottom wall: $q_B^* = q_B/\sigma(T_h^4 - T_c^4)$, where q_B is the *net surface heat flux* from the bottom wall into the medium and T_h and T_c are the temperatures of the hot and cold walls, respectively. The net surface heat flux is defined as

$$q_B = \epsilon_B \sigma T_B^4 - \epsilon_B \int_{\omega^-} I\mathbf{s} \cdot \mathbf{n}\, d\omega$$

where ϵ_B is the surface emissivity, and T_B is the temperature of the bottom wall.

4) Nondimensional temperature: $T^* = (T^4 - T_c^4)/(T_h^4 - T_c^4)$.

A. One-Dimensional Cases

The 2-D geometry for very small AR approaches a plane medium enclosed between two parallel walls which makes it possible to compare the solution with available 1-D results. To obtain the 1-D solutions, the 2-D code has been used with $AR = 1/3000$ and q_B^* is reported at the center of the bottom wall.

1. Case 1

The first problem is to find the radiative heat transfer in a purely isotropically scattering medium ($\Omega = 1$, $\Phi = 1$) contained between two black walls where the top wall is cold $T_T = T_c = 0$ K and the bottom wall is hot $T_B = T_h = 100$ K. The medium is in radiative equilibrium. Heaslet and Warming [24] have presented the exact solution for this problem. Accuracy is examined by using coarse grids $(N_x \times N_y) \times (N_\theta \times N_\phi) = (5 \times 8) \times (1 \times 16)$, where $N_\theta = 1$ means that each solid angle covers the complete range of the polar angle ($0 \le \theta \le \pi$). Four levels are used in the multigrid solver where $B_x \times B_y = 1 \times 2$.

Figure 2 compares the q_B^* values predicted by the Q_L method with the exact solution and results of the P_1 and finite volume methods for a wide range of optical thicknesses $[10^{-2} \le (\kappa^* = \sigma^s L_y) \le 10^3]$. This comparison shows that the FVM accurately predicts the radiative heat transfer in optically thin media, but the accuracy of the solution degrades as the optical thickness increases. The slow convergence rate in the optically thick limit (see Fig. 3) may suggest that this inaccuracy is a result of an unconverged solution. Convergence was checked by driving the residual R/R^o to 10^{-10} or smaller, and no significant change in q_B^* was found. The cause is the deterioration in the accuracy of the UDS when the medium is strongly participating because the significant change in intensity between the upstream node and the integration point is not accounted for. The FVM results, with UDS, approach the exact solution with spatial grid refinement at the expense of more cost and memory. The P_1 model performs surprisingly well in this 1-D problem (the maximum error is about 3.5%), a behavior which has been observed before; the reason is the semi-isotropic intensity distribution in this 1-D problem [25].

The Q_L method gives a very accurate solution for these coarse spatial and angular grids, with the maximum error of around 1.5%. It

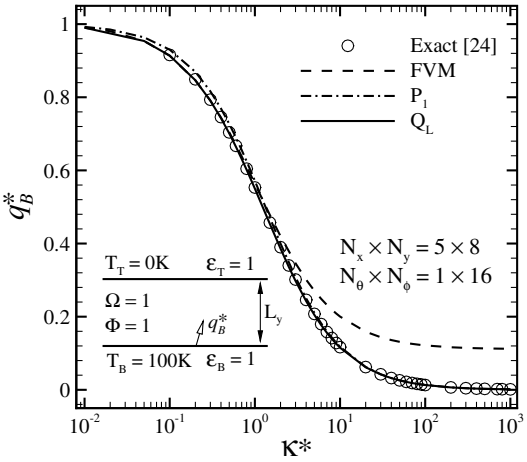

Fig. 2 Nondimensional heat flux from the bottom wall for an isotropically scattering plane medium between black walls (case 1).

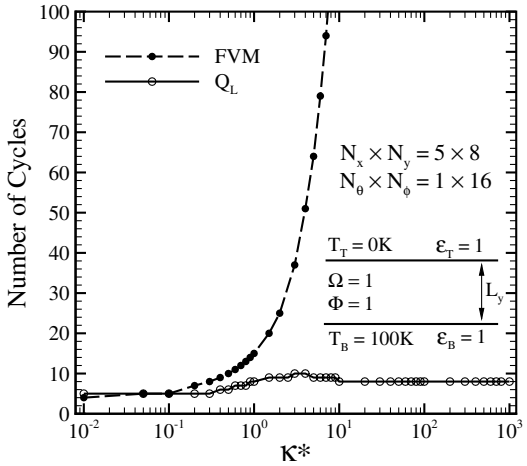

Fig. 3 Number of cycles required to achieve convergence for an isotropically scattering plane medium between black walls (case 1).

may seem strange that the FVM has a poor accuracy in the optically thick limit, while the Q_L method, which obtains the α^l distribution from the FVM, gives very accurate results. The FVM does predict a nearly isotropic intensity distribution, but the error arises because both I^l and I_a have the wrong level. This error cancels when $\alpha^l = I^l/I_a$ is calculated, so that an accurate α^l distribution ($\alpha^l \approx 1$) is passed to the Q_L equations. Furthermore, the Q_L method calculates the radiant heat flux at the integration points [Eq. (26)] by a second-order approximation which leads to an accurate calculation of the radiative heat transfer.

Figure 3 shows the number of cycles required to achieve convergence for the FVM and the Q_L method. The number of cycles for the FVM increases sharply for $\kappa^* \ge 1$ because of the strong interdirectional coupling of intensities as a result of the scattering. The convergence of the Q_L method depends on the number of cycles to establish the correct α^l distribution that is passed from the FVM to the Q_L equations. For an optically thin medium, the directional coupling is weak so the converged α^l values are obtained in only a few cycles, as seen from the FVM results in Fig. 3. In the optically thick limit, the FVM produces $\alpha^l \approx 1$ in only a few cycles, based on the I_a passed from the Q_L solution. The Q_L method therefore converges quickly for both small and large values of κ^*. The maximum number of cycles (10) occurred for the intermediate optical thicknesses ($\kappa^* = 4$ and 5).

Case 1 has been solved for partially reflecting walls ($\epsilon_B = \epsilon_T = 0.1$) and the same trends as shown in Figs. 2 and 3 were observed [20].

Note that, based on the definition of the Q_L cycle, the P_1 model converges in one cycle. Because the computational cost of each cycle

is different in these three methods, the number of cycles is not an appropriate indicator of the cost of each method. The solution cost is better measured in work units, which are reported for 2-D problems.

2. Case 2

The second case is radiative heat transfer in an emitting–absorbing isothermal slab ($\Omega = 0$) which is contained between two parallel black walls. The medium is maintained at $T_G = 50$ K and the top and bottom walls are at the same temperature $T_T = T_B = 100$ K. In this case, q_B^* is defined as $q_B^* = q_B/\sigma(T_B^4 - T_G^4)$. A relatively finer spatial grid $N_x \times N_y = 5 \times 16$ (with $B_x \times B_y = 1 \times 2$) has been used for this problem to capture the sharp variations near the walls.

Figure 4 compares the results of the Q_L, P_1, and finite volume methods with the exact solution obtained from Modest [2]. These results show that all of the three methods predict the radiative heat transfer accurately for the optically thin media but the accuracy of the P_1 model degrades rapidly as the absorption coefficient increases. The poor accuracy of the P_1 model is caused by the temperature jump, and hence an intensity jump, at the wall [2]. The maximum error in the Q_L and finite volume predictions is about 4% whereas the P_1 model has a maximum error of 15%. There is very fast convergence for any optical thickness since the directional intensities are decoupled: the FVM converges in two cycles, and the Q_L method requires four cycles.

B. Two-Dimensional Cases

In this section, the Q_L method is extended to 2-D test cases. In all cases, the medium is in radiative equilibrium. One work unit (WU) for a specific set of spatial and angular grids is defined as the computational time required to do 10 explicit updates in the FVM on that grid (i.e., 10 FVM cycles). The solution cost in WU is found by dividing the CPU time for the solution by the CPU time for 10 FVM cycles. Reporting work units is better than CPU time itself because the results are more independent of the computer speed and the grid used.

1. Case 3

The first 2-D test case is a purely isotropically scattering medium ($\Omega = 1$, $\Phi = 1$) enclosed in a square enclosure ($AR = 1$) where the bottom wall is hot $T_B = T_h = 100$ K and the other three walls are cold $T_c = 0$ K. The exact solution of this problem has been presented by Crosbie and Schrenker [26]. The spatial grid is $N_x \times N_y = 27 \times 27$ with four levels in the multigrid solver ($B_x \times B_y = 3 \times 3$). $N_\theta \times N_\phi = 1 \times 24$ solid angles have been used for the angular discretization.

Figure 5 compares the q_B^* along the first half of the bottom wall predicted by the Q_L method with the exact solution and results of the FVM and P_1 model for three optical thicknesses: $\kappa^* = 0.25$, 1, and 10. The P_1 model greatly overpredicts the heat transfer for $\kappa^* = 0.25$

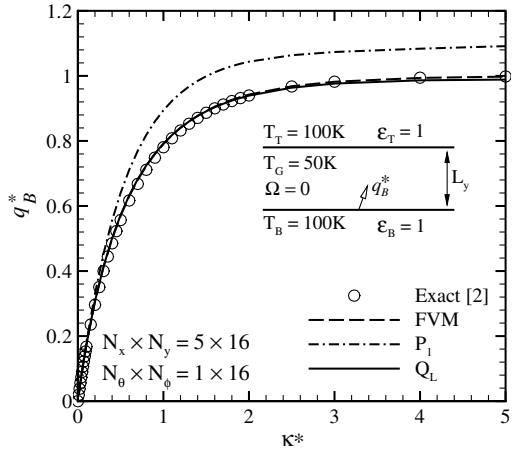

Fig. 4 Nondimensional heat flux from the bottom wall of an isothermal emitting–absorbing slab with black walls (case 2).

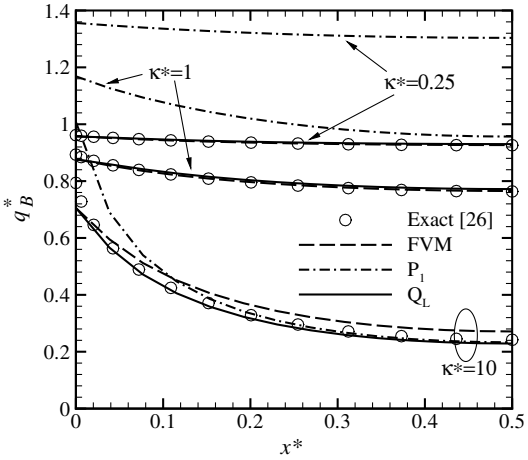

Fig. 5 Nondimensional heat flux from the bottom wall for an isotropically scattering medium in a square enclosure with black walls (case 3).

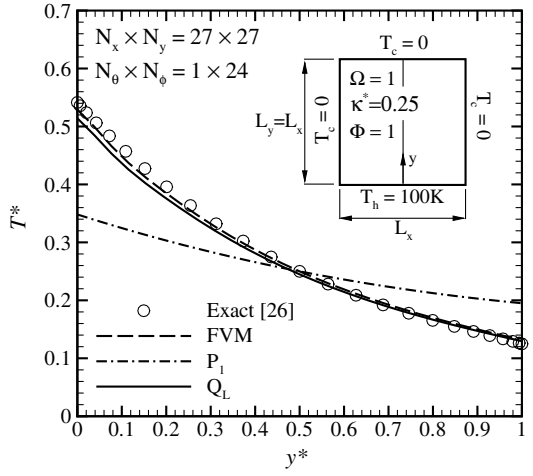

Fig. 6 Nondimensional temperature along the centerline for an isotropically scattering medium in a square enclosure with black walls for $\kappa^* = 0.25$ (case 3).

and 1, especially near the corner where a discontinuity in the surface emissive power exists. This discontinuity also affects the accuracy of the P_1 predictions for $\kappa^* = 10$. The FVM accurately predicts the radiative heat transfer except for the optically thick medium, where UDS is inaccurate, as discussed in case 1. The Q_L method yields very accurate q_B^* distributions for all of these three small, medium, and large optical thicknesses for this set of coarse grids.

Figure 6 shows T^* along the centerline for $\kappa^* = 0.25$. The temperature distribution has been obtained from $I_b = I_a$ as a result of the radiative equilibrium. For $\kappa^* = 1$ and 10, not presented here, the P_1 prediction approaches the exact solution whereas the FVM solution deviates from the exact results as κ^* increases. For all optical thicknesses, the Q_L prediction for T^* is in very good agreement with the exact results.

Figure 7 quantifies the error in the solution of the FVM, the Q_L method, and the P_1 model for a wide range of optical thickness. Results are reported for $(N_x \times N_y) \times (N_\theta \times N_\phi) = (27 \times 27) \times (1 \times 24)$, with four levels in the multigrid solver ($B_x \times B_y = 3 \times 3$). The error in the predicted q_B^* at the center of the bottom wall has been calculated as

$$q_B^* \text{ error} = \frac{|q_{B,\text{exact}}^* - q_{B,\text{predicted}}^*|}{q_{B,\text{exact}}^*} \times 100$$

where $q_{B,\text{exact}}^*$, if not reported in [26], is obtained by extrapolating the results from three spatial grids: 27×27, 81×81, and 243×243.

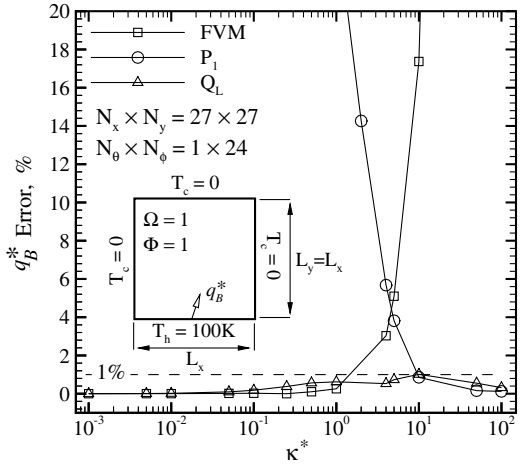

Fig. 7 Percentage error in the predicted heat flux from the center of the bottom wall in an isotropically scattering medium in a square enclosure with black walls (case 3).

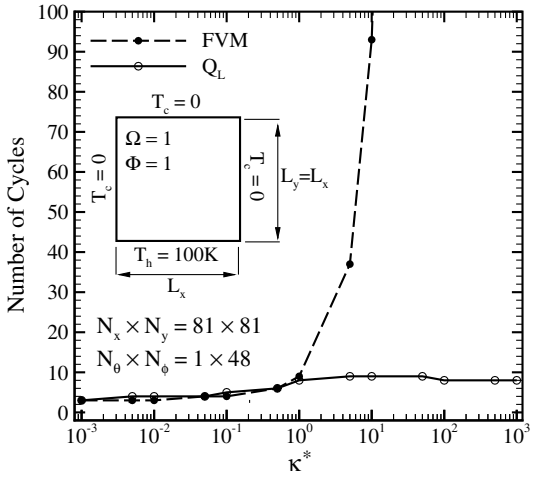

Fig. 9 Number of cycles required to achieve convergence for the FVM and Q_L method applied to an isotropically scattering medium in a square enclosure with black walls (case 3).

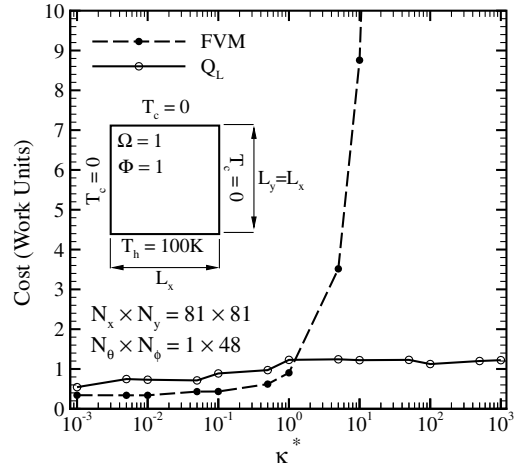

Fig. 8 Solution cost of the FVM and Q_L method applied to an isotropically scattering medium in a square enclosure with black walls (case 3).

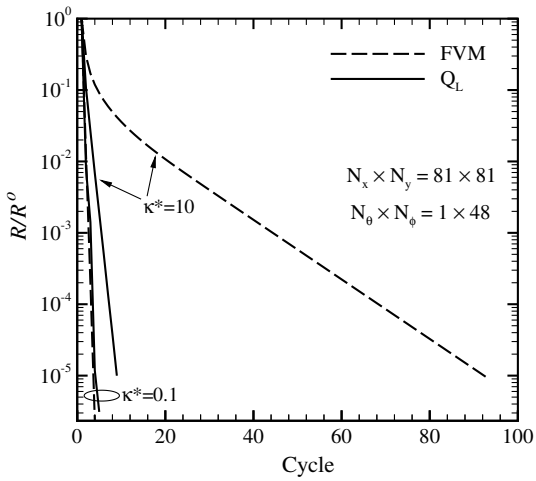

Fig. 10 Residual reduction history of the Q_L method and the FVM for $\kappa^* = 0.1$ and 10 (case 3).

Figure 7 shows that the error of the Q_L method is always less than 1%, whereas the P_1 model and the FVM achieve this accuracy only for $\kappa^* \geq 10$ and $\kappa^* \leq 1$, respectively. The poor performance of the P_1 model in the optically thin media is because in this limit, the intensity varies strongly with direction.

For this test case, Figs. 8 and 9 compare the solution cost and number of cycles, respectively, for the finite volume and Q_L methods for a wide range of optical thickness. Results are reported for a set of fine spatial and angular grids $(N_x \times N_y) \times (N_\theta \times N_\phi) = (81 \times 81) \times (1 \times 48)$ with $B_x \times B_y = 3 \times 3$.

These figures show that the Q_L solution converges in less than 10 cycles and the solution cost is around 1 WU for the whole range of the medium participation. The FVM has a lower solution cost for the optically thin media, as already explained; but the cost and number of cycles of the FVM rises sharply for $\kappa^* \geq 1$ because of the increase in interdirectional coupling. The Q_L method is less costly than the FVM for $\kappa^* > 1$. The Q_L method requires more work units in the optically thin limit, but the solution cost for this limit remains small. Figure 10 depicts the scaled residual reduction history of the Q_L method, Eq. (34), and the FVM, Eq. (31), for $\kappa^* = 0.1$ and 10. Both methods reduce residuals monotonically and the Q_L method has a very fast convergence rate at both limits whereas the FVM is slow in the optically dense limit.

To demonstrate the performance of the Q_L method more clearly, Table 1 tabulates the results of Figs. 8 and 9 for some selected optical thicknesses and also for partially reflecting walls, $\epsilon_s = 0.1$ and 0.5. This table presents the number of cycles and work units for the Q_L and finite volume methods and the portion of the solution cost spent to form and solve the I_a equations for the Q_L method (the percentages in parentheses). This portion decreases with increasing optical thickness, because for large κ^*, the I_a equations are more strongly diagonally dominant and therefore, the multigrid solver converges faster. Table 1 illustrates the very good performance of the Q_L method; the solution cost in work units is almost constant and independent of κ^*. The efficacy of the Q_L method is noticeable for the strongly participating media and strongly reflecting boundaries; it is more costly than the FVM only in the optically thin limit and only when the walls have large emissivity.

The P_1 solution always converges in one cycle and, by using the ACM, its solution cost is comparable to the cost of the first cycle of the Q_L solution.

Nonparticipating Media: Eq. (11), used in the Q_L method, is inappropriate for $\kappa^* = 0$, as already stated. If $\kappa^* = 0$ occurs in a region of the solution domain, the Q_L method will diverge. This problem can be overcome by replacing $\kappa^* = 0$ with a small value, but this may affect accuracy. The question is, how small can κ^* be made before there are solver problems?

In this test case for $(N_x \times N_y) \times (N_\theta \times N_\phi) = (27 \times 27) \times (1 \times 24)$, using $\sigma^s = 10^{-6}$ m^{-1} ($\kappa^* = 10^{-6}$) in the Q_L method gives the q_B^* along the bottom wall for $\kappa^* = 0$ accurate to five significant digits, the solution converges within four cycles, the solution cost is 0.8 WU, and 53% of the solution cost is spent on the I_a equations. It seems that placing a lower limit on κ^* gives accurate results with a

Table 1 Solution cost of the Q_L method and FVM applied to a square enclosure with an isotropically scattering medium (case 3)

	FVM		Q_L	
κ^*	WU	Cycle	WU	Cycle
			$\epsilon_s = 1.0$	
0.1	0.5	4	0.9 (38%)[a]	5
0.5	0.6	6	1.0 (32%)	6
1.0	0.9	9	1.2 (29%)	8
5.0	3.5	37	1.2 (22%)	9
10.0	8.8	93	1.2 (20%)	9
			$\epsilon_s = 0.5$	
0.1	1.1	11	1.4 (30%)	9
0.5	1.6	16	1.4 (28%)	9
1.0	2.0	21	1.4 (24%)	10
5.0	6.2	66	1.9 (20%)	14
10.0	12.9	137	2.2 (21%)	16
			$\epsilon_s = 0.1$	
0.1	5.9	62	3.7 (26%)	25
0.5	8.1	85	2.2 (26%)	15
1.0	10.7	113	2.0 (26%)	14
5.0	30.2	320	2.8 (23%)	20
10.0	54.0	571	2.8 (23%)	20

[a]Proportion of WU required to form and solve the Q_L equations.

reasonable solution cost. However, its application to other problems still needs to be explored.

2. Case 4

In this case, the radiative heat transfers in a tall enclosure ($AR = 10$) and a wide enclosure ($AR = 1/5$) have been found by the Q_L method and the results compared with the FVM and exact solutions. As before, the bottom wall is hot $T_B = T_h = 10$ K and the other three walls are cold $T_c = 0$ K. In both cases, the optical thickness is unity ($\kappa^* = \sigma^s L_y = 1$). For $AR = 10$, $N_x \times N_y = 9 \times 25$ control volumes with $B_x \times B_y = 3 \times 5$, and for $AR = 1/5$, $N_x \times N_y = 25 \times 9$ control volumes with $B_x \times B_y = 5 \times 3$ have been employed for the spatial grid. In both cases, $N_\theta \times N_\phi = 1 \times 24$ solid angles are used for the angular discretization.

Figures 11 and 12, respectively, compare q_B^* on the first half of the bottom wall and T^* along the centerline obtained by the Q_L and finite volume methods with the exact solution of Crosbie and Schrenker [26]. For this set of coarse grids, both methods are found to have very good accuracy for the tall enclosure ($AR = 10$) where the error in the predicted q_B^* at the center of the bottom wall is 0.3 and 0.7% for the FVM and Q_L method, respectively. In this case, the optical thicknesses in both of the x and y directions are small ($\kappa_x^* = \sigma^s L_x = 0.1$), so the UDS is accurate. Notice that both methods slightly underestimate T^* near the bottom wall (hot wall); the accuracy can be improved by using a finer spatial grid (especially in the y direction).

For the wide enclosure ($AR = 1/5$), the FVM suffers from the inaccuracy of the UDS because in this case, $\kappa_x^* = 5\kappa_y^* = 5$ and the medium is optically dense in the x direction. The error in the prediction of the FVM for q_B^* at the center of the bottom wall is around 3%. The Q_L method gives very accurate results for this case too, with 0.1% error in q_B^* at the center of the wall.

To study the cost of the Q_L method for rectangular enclosures, the radiative heat transfer in a wide enclosure with $AR = 1/10$ has been solved by the Q_L method and FVM, and the work units and number of cycles have been reported in Table 2. This aspect ratio has been chosen because its convergence rate is worse than for $AR = 10$ or $1/5$. A set of fine grids $(N_x \times N_y) \times (N_\theta \times N_\phi) = (125 \times 27) \times (1 \times 48)$ has been used for the spatial and angular grids with $B_x \times B_y = 5 \times 3$ (four levels). These results show the advantage of the Q_L method over the FVM and the enormous reduction in the solution cost for the optically thick limit. The cost penalty for the Q_L method in the optically thin limit is a little larger than before (0.7 WU), mainly because of the larger portion of the cost spent on solving the

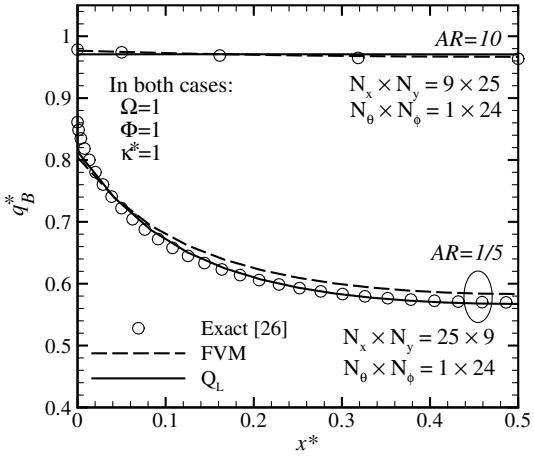

Fig. 11 Nondimensional heat flux from the bottom wall for an isotropically scattering medium with unit optical thickness in rectangular enclosures with black walls (case 4).

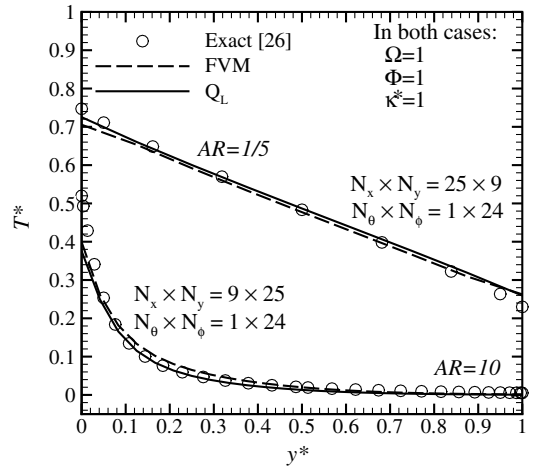

Fig. 12 Nondimensional temperature along the centerline for an isotropically scattering medium with unit optical thickness in rectangular enclosures with black walls (case 4).

I_a equations with the multigrid solver (≈48%). This is probably caused by the small aspect ratios of the coarse-mesh blocks.

3. Case 5

Excellent convergence obtained for a range of grid resolution and optical thickness may be misleading, because for other combinations the same method may lead to poor convergence or even divergence. Poor convergence was observed [11,14] for the mesh rebalance method for fine meshes and cell optical thickness (based on the grid length scale Δ) between 0.1 and 1. To check that the performance of the Q_L method does not unexpectedly degrade, case 3 (involving scattering only), is solved for $0.001 \leq \sigma^s \Delta \leq 100$, and for grid sizes $N_x \times N_y$ from 4×4 to 128×128. The grid length scale Δ is calculated here as $\Delta = L_x/(N_x - 1)$ (width of the interior control

Table 2 Solution cost of the Q_L method and FVM applied to an isotropically scattering medium in a wide enclosure with black walls (case 4)

	FVM		Q_L	
κ^*	WU	Cycle	WU	Cycle
0.1	0.5	5	1.2 (48%)[a]	6
0.5	0.9	9	1.0 (35%)	6
1.0	1.3	13	1.2 (28%)	8
5.0	6.2	65	1.6 (26%)	11
10.0	15.4	163	1.3 (21%)	10

[a]Proportion of WU required to form and solve the Q_L equations.

Table 3 The solution cost and number of cycles required by the Q_L method applied to a square enclosure with black walls enclosing an isotropically scattering medium (case 5)

	$N_x \times N_y$				
$\sigma^s \Delta$	4×4	8×8	32×32	64×64	128×128
0.001	3[a] [0.4][b] (0%)[c]	3 [0.4] (19%)	4 [0.6] (28%)	4 [0.7] (33%)	5 [1.0] (43%)
0.01	4 [0.5] (0%)	4 [0.6] (27%)	5 [0.7] (25%)	6 [1.0] (30%)	8 [1.2] (32%)
0.1	5 [0.6] (0%)	7 [1.0] (27%)	9 [1.2] (21%)	9 [1.2] (21%)	10 [1.4] (23%)
1	8 [1.0] (0%)	8 [1.1] (24%)	9 [1.2] (20%)	9 [1.2] (21%)	9 [1.3] (26%)
10	7 [0.9] (0%)	8 [1.0] (18%)	8 [1.1] (19%)	8 [1.2] (24%)	8 [1.3] (32%)
100	7 [0.6] (0%)	8 [1.0] (14%)	8 [1.1] (21%)	8 [1.2] (26%)	8 [1.3] (35%)

[a]Number of cycles.
[b]Number of work units.
[c]Proportion of WU required to form and solve the Q_L equations.

volumes). $N_\theta \times N_\phi = 1 \times 48$ solid angles have been used in the angular grid. Coarse-mesh blocks are $B_x \times B_y = 2 \times 2$.

Table 3 presents the number of cycles, work units (in square brackets), and the portion of the solution cost spent to form and solve the Q_L equations (in parentheses). These results illustrate the good convergence rate of the Q_L method for the range of very coarse to very fine grids and for a wide range of optical thickness. The computational cost required to form and solve the Q_L equations is around 20–25% of the total solution cost, except for very small optical thicknesses where solving the I_a equations is costly due to the lack of diagonal dominance.

IV. Discussion

The focus of the FVM or DOM is the solution for the directional intensities I^l. The solution for the average intensity I_a is used only to accelerate the solution of the I^l equations; such acceleration methods have never proved to be generally successful. In contrast, the main focus of the Q_L method is solution for the average intensity I_a. The directional intensities I^l are only obtained to update the α^l parameters that appear in the I_a equations. Here the values of α^l were obtained from the FVM, but they could be obtained from the DOM or some other model. The Q_L method changes the solution paradigm by reversing the roles of the I_a and I^l equations.

The Q_L method has been shown to provide solutions to radiation problems with computational effort that is only weakly dependent on the strength of medium participation, scattering phase function, and wall reflectivity. The FVM with UDS is less expensive for weakly participating media when solving only for radiation, but is not practical at all for strongly participating media. The accuracy of the Q_L method is as good as, or for strong medium participation better than, the FVM with UDS.

Although the accuracy of the Q_L method can be better than for the FVM with UDS, and the discretization is $\mathcal{O}(\Delta^2)$, it still converges with $\mathcal{O}(\Delta)$ with grid refinement. This is because the α^l values have $\mathcal{O}(\Delta)$ accuracy. If second-order accuracy with grid refinement is required, then an $\mathcal{O}(\Delta^2)$ scheme must be used in the FVM equations that supply the values of α^l. This is simple to implement.

The average intensity I_a in the Q_L method is related to all neighbor nodes, so the bandwidth of the I_a equation is large. In addition, the I_a equations are not always diagonally dominant. No difficulty was experienced when multigrid was used to solve these equations, but both features are undesirable when the Q_L method is used in a general-purpose CFD code where robustness and cost are top priorities. It should be possible to form a reduced bandwidth equation that is diagonally dominant, and to lag the difference between the full and reduced bandwidth equations. This remains to be examined.

There is good reason to expect that the real cost advantage of the Q_L method will occur when it is implemented in a CFD code in which radiation is but one of many coupled processes. The Q_L method includes radiation through the inclusion of a single equation, as with the P_1 model. This permits robustness to be increased by solving for I_a and temperature using a coupled solver. The distribution of α^l need only be updated at a frequency specified by the analyst, perhaps every 10 or 20 time steps. For preliminary calculations, leaving α^l at its initialized value, $\alpha^l = 1$, may be sufficient because this yields results similar to the P_1 model. The update of α^l using the FVM is very inexpensive because the equations are not directionally coupled and can therefore be formed and solved in a single sweep of the grid. Because of the lack of coupling, the I^l equations can be easily formed and solved in parallel, using memory that does not conflict with the solution of other equations. Compared to the P_1 model, to form and solve the I_a equations for L directions and $N_x \times N_y$ nodes in a 2-D problem requires $(L + 5) \times (N_x \times N_y) + 7L$ extra words of computer memory in the Q_L method (for α^l, T_{ij}, S_i, N_i^l, D_{ij}^l, and F_i^l). When applied in a general-purpose CFD code, where convergence is limited by other processes, the Q_L solution for radiation should approach the accuracy of the FVM at a cost not much greater than for the P_1 model.

V. Conclusions

This paper introduces the Q_L method for computing thermal radiation in participating media. It solves a single equation for the average intensity I_a, and accounts for the directional distribution of intensities through parameters α^l, one for each solid angle. If a value of $\alpha^l = 1$ is specified for each solid angle, the Q_L method reduces to the P_1 model at interior nodes. Better values of α^l can be provided from a FVM or DOM solution for the directional intensities.

The cost of obtaining a solution by the Q_L method was shown to be slightly higher than the FVM for small optical thickness, but becomes much less costly as the medium becomes optically dense. The accuracy of the Q_L method, when UDS is used to provide the α^l values, is as good as or better than that of the FVM with UDS. When used in the Q_L method, the solution of the FVM equations is very fast because only one sweep of the angular and spatial grids is needed for each update of the α^l values.

The Q_L method fails for transparent media, but using a lower limit as small as $\kappa^* = 10^{-5}$ results in good agreement with the $\kappa^* = 0$ solution, and the Q_L method converges rapidly.

The Q_L method still needs to be implemented and benchmarked in a CFD code involving multiprocesses. It has been argued, but not proved, that the Q_L method should approach the accuracy of the FVM at a cost approaching that of the P_1 model.

Acknowledgments

This work was financially supported by the Climate Change Technology and Innovation Initiative (CCTII) through CANMET Energy Technology Centre, Natural Resources Canada, of the Canadian Federal Government, and through an operating grant to the second author from the Natural Sciences and Engineering Council of Canada. The authors also gratefully acknowledge the contributions of G. D. Stubley.

References

[1] Viskanta, R., and Mengüç, M. P., "Radiation Heat Transfer in Combustion Systems," *Progress in Energy and Combustion Science*, Vol. 13, No. 2, 1987, pp. 97–160. doi:10.1016/0360-1285(87)90008-6

[2] Modest, M. F., *Radiative Heat Transfer*, 2nd ed., Academic Press, New York, 2003.
[3] Fiveland, W. A., "Discrete-Ordinates Solutions of the Radiative Transport Equation for Rectangular Enclosures," *Journal of Heat Transfer*, Vol. 106, No. 4, 1984, pp. 699–706.
[4] Fiveland, W. A., "Discrete Ordinate Methods for Radiative Heat Transfer in Isotropically and Anisotropically Scattering Media," *Journal of Heat Transfer*, Vol. 109, No. 3, 1987, pp. 809–812.
[5] Truelove, J. S., "Discrete-Ordinate Solutions of the Radiation Transport Equation," *Journal of Heat Transfer*, Vol. 109, No. 4, 1987, pp. 1048–1051.
[6] Fiveland, W. A., "Three-Dimensional Radiative Heat Transfer Solutions by the Discrete-Ordinates Method," *Journal of Thermophysics and Heat Transfer*, Vol. 2, No. 4, 1988, pp. 309–316.
[7] Raithby, G. D., and Chui, E. H., "A Finite-Volume Method for Predicting a Radiant Heat Transfer in Enclosures with Participating Media," *Journal of Heat Transfer*, Vol. 112, No. 2, 1990, pp. 415–423.
[8] Chui, E. H., and Raithby, G. D., "Computation of Radiant Heat Transfer on a Nonorthogonal Mesh Using the Finite Volume Method," *Numerical Heat Transfer*, Vol. 23, No. 3, 1993, pp. 269–288. doi:10.1080/10407799308914901
[9] Chai, J. C., Lee, H. S., and Patankar, S. V., "Finite Volume Method for Radiation Heat Transfer," *Journal of Thermophysics and Heat Transfer*, Vol. 8, No. 3, 1994, pp. 419–425.
[10] Murthy, J. Y., and Mathur, S. R., "Finite Volume Method for Radiative Heat Transfer Using Unstructured Meshes," *Journal of Thermophysics and Heat Transfer*, Vol. 12, No. 3, 1998, pp. 313–321.
[11] Fiveland, W. A., and Jessee, J. P., "Acceleration Schemes for the Discrete Ordinates Method," *Journal of Thermophysics and Heat Transfer*, Vol. 10, No. 3, 1996, pp. 445–451.
[12] Cefus, G. R., and Larsen, E. W., "Stability Analysis of Coarse-Mesh Rebalance," *Nuclear Science and Engineering*, Vol. 105, No. 1, 1990, pp. 31–39.
[13] Chui, E. H., and Raithby, G. D., "Implicit Solution Scheme to Improve Convergence Rate in Radiative Transfer Problems," *Numerical Heat Transfer*, Vol. 22, No. 3, 1992, pp. 251–272. doi:10.1080/10407799208944983
[14] Raithby, G. D., and Chui, E. H., "Accelerated Solution of the Radiation-Transfer Equation with Strong Scattering," *Journal of Thermophysics and Heat Transfer*, Vol. 18, No. 4, 2004, pp. 156–159.
[15] Mathur, S. R., and Murthy, J. Y., "Coupled Ordinates Method for Multigrid Acceleration of Radiation Calculations," *Journal of Thermophysics and Heat Transfer*, Vol. 13, No. 4, 1999, pp. 467–473.
[16] Mathur, S. R., and Murthy, J. Y., "Acceleration of Anisotropic Scattering Computations Using Coupled Ordinates Method (COMET)," *Journal of Heat Transfer*, Vol. 123, No. 3, 2001, pp. 607–612. doi:10.1115/1.1370506
[17] Chui, E. H., Raithby, G. D., and Hughes, P. M. J., "Prediction of Radiative Heat Transfer in Cylindrical Enclosures with the Finite Volume Method," *Journal of Thermophysics and Heat Transfer*, Vol. 6, No. 4, 1992, pp. 605–611.
[18] Chai, J. C., Patankar, S. V., and Lee, H. S., "Evaluation of Spatial Differencing Practices for the Discrete-Ordinates Method," *Journal of Thermophysics and Heat Transfer*, Vol. 8, No. 1, 1994, pp. 140–144.
[19] Jessee, J. P., and Fiveland, W. A., "Bounded, High-Resolution Differencing Schemes Applied to the Discrete Ordinates Method," *Journal of Thermophysics and Heat Transfer*, Vol. 11, No. 4, 1997, pp. 540–548.
[20] Hassanzadeh, P., "An Efficient Computational Method for Thermal Radiation in Participating Media," M.Sc. Thesis, University of Waterloo, Ontario, Canada, June 2007, http://hdl.handle.net/10012/3135.
[21] Schneider, G. E., and Raw, M. J., "Control Volume Finite-Element Method for Heat-Transfer and Fluid-Flow Using Colocated Variables. 1. Computational-Procedure," *Numerical Heat Transfer*, Vol. 11, No. 4, 1987, pp. 363–390. doi:10.1080/10407788708913560
[22] Hutchinson, B. R., and Raithby, G. D., "A Multigrid Method Based on the Additive Correction Strategy," *Numerical Heat Transfer*, Vol. 9, No. 5, 1986, pp. 511–537. doi:10.1080/10407788608913491
[23] Briggs, W. L., *A Multigrid Tutorial*, 1st ed., SIAM, Philadelphia, PA, 1987.
[24] Heaslet, M. A., and Warming, R. F., "Radiative Transport and Wall Temperature Slip in an Absorbing Planar Medium," *International Journal of Heat and Mass Transfer*, Vol. 8, No. 7, 1965, pp. 979–994. doi:10.1016/0017-9310(65)90083-9
[25] Bayazitoğlu, Y., and Higenyi, J., "Higher-Order Differential Equations of Radiative Transfer: P_3 Approximation," *AIAA Journal*, Vol. 17, No. 4, 1979, pp. 424–431.
[26] Crosbie, A. L., and Schrenker, R. G., "Radiative Transfer in a Two-Dimensional Rectangular Medium Exposed to Diffuse Radiation," *Journal of Quantitative Spectroscopy and Radiative Transfer*, Vol. 31, No. 4, 1984, pp. 339–372. doi:10.1016/0022-4073(84)90095-5